Additively manufactured equiatomic CoCrFeMnNi high entropy alloy: Precipitation-induced heterogeneity by mechano-chemical coupling

Shabnam Taheriniya,[1] Nuri Choi,[1] Sangsun Yang,[2] Reshma Sonkusare,[3] Ji Hun Yu,[2] Jai-Sung Lee,[4] Harald Rösner,[1] Martin Peterlechner,[1] Torben Boll,[3] Christoph Gammer,[5] Horst Hahn,[6] Sergiy V. Divinski,[1] and Gerhard Wilde[1]

[1] *University of Münster, Institute of Materials Physics, Wilhelm-Klemm-Str. 10, 48149 Münster, Germany*
[2] *Powder Materials Division, Korea Institute of Materials Science, Changwon, 51508,South Korea*
[3] *Institute of Applied Materials (IAM-WK), Institute for Nanotechnology (INT) and Karlsruhe Nano Micro Facility (KNMF), Karlsruhe Institute of Technology, 76344 Eggenstein-Leopoldshafen, Germany*
[4] *Department of Materials Science and Chemical Engineering, Hanyang University, 15588 Ansan, South Korea*
[5] *Erich Schmid Institute of Materials Science, Austrian Academy of Sciences, Jahnstraße 12, 8700 Leoben, Austria*
[6] *Institute for Nanotechnology (INT), Karlsruhe Institute of Technology, 76344 Eggenstein-Leopoldshafen, Germany*

(Dated: November 28, 2024)

Additive manufacturing via selective laser melting of gas-atomized equiatomic powder was used to fabricate a CoCrFeMnNi high-entropy alloy. Analytical transmission electron microscopy, nanobeam diffraction, atom probe tomography and nanoindentation were employed to provide a comprehensive overview on the evolution of microstructure and nano-hardness upon annealing at a moderate temperature of 550°C motivated by a maximum heat release at that temperature. A complex mechano-chemical coupling was observed, which leads to segregation and phase separation at grain boundaries. The as-manufactured material contained alternating regions of equiaxed and columnar grains. The corresponding microstructure is composed of high-angle grain boundaries and intrinsic dislocation networks, which displayed heterogeneous segregation of Mn and to some extent Ni. Longer annealing led to Cr enrichment at high-angle grain boundaries, and later to a phase separation with neighboring Cr-rich and MnNi-rich regions. Synergetic effects of segregation, nano-precipitation and dislocation accumulation at high-angle grain boundaries give rise to built up stresses which increase and homogenize hardness in the 3D-printed CoCrFeMnNi alloy.

Keywords: additive manufacturing; high-entropy alloy; transmission electron microscopy; strain mapping, segregation

1. INTRODUCTION

The performance of high entropy alloys (HEAs), as a new class of materials with multi-principal elements and high configuration entropy[1], is eminent in terms of high strength, high fracture toughness, corrosion resistance, and thermal stability[2]. The conventional methods applied for the manufacturing of bulk high entropy alloys are mainly casting and plasma sintering, which can only produce rough parts in simple shapes. Additive manufacturing methods, such as selective laser melting (SLM) or laser powder bed fusion (LPBF), have shown promising results in the manufacturing of three-dimensional (3D) materials of complex shapes featuring superior mechanical properties[3]. The application of controllable high energy laser beams that fuse metallic powder layer by layer has not only increased the freedom to design difficult-to-machine materials such as HEAs, but has also been proven to be affordable and efficient for manufacturing complex structures with high geometric accuracy and low surface roughness. While HEAs produced by the SLM method are known to contain void-type defects, residual stresses, cracks and element segregation, these defects can be handled by optimizing the processing parameters, i.e. using artificial intelligence[4–6].

A single phase CoCrFeMnNi alloy (also known as Cantor alloy[7]) with a face-centered-cubic (FCC) crystal structure[8] is generally recognized as a 'model' HEA, and has been associated with an ideal combination of strength and ductility at high and cryogenic temperatures[9,10]. According to Otto et al.[9], the grain boundary hardening through grain refinement from 144 to 4.4 μm increases the room-temperature yield strength of the Cantor alloy from 200 to 350 MPa; precipitation hardening can further improve the strength without undermining the ductility[11]. The results of contemporary research on 3D-printed equiatomic CoCrFeMnNi alloy show an excellent printability[12], uniform high hardness, increased yield and tensile strength[13–15], non-equilibrium solidification microstructures and anisotropic mechanical properties[16]. Furthermore, the strength and ductility of the 3D-printed FCC CoCrFeMnNi exhibit a simultaneous enhancement at cryogenic temperatures[13]. Kim et al.[17] observed an excellent yield strength and fatigue resistance in the SLM-built CoCrFeMnNi.

The essential factors for the improved mechanical performance were intrinsic microstructural defects, such as heterogeneous grain structure, dislocation networks, in-situ formed oxides and deformation twins generated during cyclic processing[17]. To achieve a high density and a high chemical homogeneity, Haase et al. used elemental powder blends to produce CoCrFeMnNi alloys via laser metal deposition (LMD) processing[18]. The experimetal results showed that the mechanical properties of the alloy under uniaxial compression were superior to the conventionally processed HEAs due to the absence of macro-

segregation[18]. The 3D-printed CoCrFeMnNi alloy revealed anisotropic mechanical properties with a higher yield strength but lower elongation until failure along the build direction compared to the laser scan direction[16]. Furthermore, an anisotropy was observed for the corrosion resistance with respect to the build and laser scan directions[16].

The thermally induced segregation and the effect of post-annealing (800°C and 900°C) on the microstructure and mechanical properties of SLM-processed interstitial CoCrFeMnNi-1at.%C alloy were investigated by Park et al.[19]. The heat-treated C-alloyed HEA retains a high dislocation density and exhibits an impediment of grain boundary migration by $Cr_{23}C_6$ carbide and carbon interstitials. This combination leads to superior tensile properties as opposed to the as-built C-HEA[19].

The SLM-manufactured alloys tend to have a heterogeneous grain structure composed of alternating equiaxed and columnar grain areas that grow in the specific pattern resulting from regular variations of local thermal gradients[20]. The microstructure is composed of high-angle grain boundaries (HAGBs) and dislocation networks forming sub-boundaries upon the solidification process[12]. The superior mechanical properties of the SLM-produced CoCrFeMnNi alloy are due to segregation at HAGBs and the nano-sized cellular substructures[2122]. This maximizes the strength in combination with the homogeneously nano-sized precipitates located at different grain boundaries and inside the grains[17,23]. Equilibrium phases and pronounced crystallographic texture resulting from high cooling rates can be modified by post-LMD heat treatment and varying scan strategies[18].

Radiotracer grain boundary diffusion measurements in 3D-printed CoCrFeMnNi HEA revealed evidence attributed to a 'non-equilibrium' state of HAGBs, which is characterized by diffusion rates that are enhanced by orders of magnitude[24]. The 'non-equilibrium' state is found to relax completely after annealing at 500°C[24]. The same SLM-built equiatomic CoCrFeMnNi alloy, which was used in the radiotracer diffusion study[24], is in the focus of this work, which thoroughly examines the microstructure in the as-prepared and heat-treated states (annealed at 550°C for 1 or 10 h). The chosen annealing temperature of 550°C was motivated by differential scanning calorimetry (DSC) revealing a maximum heat release at this temperature. The evolution of the elemental distribution, dislocation density and the corresponding nano-hardness are investigated with special focus on strain accumulation at HAGBs upon annealing. The comprehensive results which differentiate between regions of columnar and equiaxed grains provide deep insight into the complex interplay of segregation, phase decomposition and strain, which constitutes mechano-chemical coupling.

2. EXPERIMENTAL DETAILS

2.1. Sample production

The CoCrFeMnNi HEA specimens were produced by additive manufacturing at the Korean Institute of Materials Science (KIMS, Changwon, South Korea). A cast and homogenized ingot with the required equiatomic composition was first gas-atomized at 1580°C in argon atmosphere to produce an equiatomic micrometer-large alloy powder. The argon pressure was controlled between 50 and 70 bar. The powder was classified using test sieves and aerosol classifier yielding particle diameters in the range of 10 μm to 45 μm which subsequently was additively manufactured using a selective laser melting (SLM) process (MLab Cusing, supplied by Concept Laser GmbH). During the processing, a layer of the classified Cantor alloy powder was spread on a stainless-steel baseplate using a rubber blade to produce disc-shaped samples with a diameter of 10 mm and a thickness of 2 mm. The thickness of each powder layer was set to 25 μm, while the fiber laser scanned the powder bed with a laser power of 90 W. The scan speed and hatch space were 600 mm/s and 77 μm, respectively. The average relative density of the obtained samples was measured to be $(99.4^{+0.5}_{-1.7})\%$.

2.2. Microstructure analysis of the powder and SLM-built sample

The chemical composition of the powder particles and the grain structure of the additively manufactured CoCrFeMnNi alloy were studied by means of energy dispersive spectroscopy (EDS) and electron back scattered diffraction (EBSD) using an FEI Nano Nova SEM 230. For this purpose, the powder was embedded in epoxy resin and polished in order to reveal an accurate view of the microstructure. The preparation of the investigated surfaces involved mechanical grinding using abrasive SiC papers and mechanical polishing by 3 μm diamond suspensions followed by a final step with oxide polishing suspension (OPS) to obtain a mirror like finish. The microstructure of the bulk sample and the embedded powder was investigated by the EBSD method using an acceleration voltage of 20 kV, aperture size of 60 μm, working distance of 15 mm while the sample was tilted to 70°.

2.3. DSC measurements and heat treatment

The thermally induced phase transitions in the as-manufactured state were investigated in a PerkinElmer DSC-7 calorimeter using a constant heating rate of 20 K/min. The heat treatments were carried out on cylindrical disks of 3 mm in diameter sealing them in quartz tubes filled with purified Ar.

2.4. Micro and nano-hardness measurements

The Vickers microhardness (HV) measurements were performed on samples in as-printed and heat-treated states using a micro-indenter (Bühler). High-resolution hardness maps of the as printed and heat-treated samples were recorded with a continuous stiffness measurement (CSM) method, using a FemtoTools FT-NMT04 nanoindenter equipped with a calibrated Berkovich diamond tip and micro-force sensing probe and 200 mN maximal force. A loading speed of 0.1 μm/s with a harmonic frequency of 200 Hz and an amplitude of 5 nm was set for the recording of the CSM maps. The indents were 200 nm deep with 2 μm step size between the indents. Moreover, the sample surfaces were polished to a mirror like finish prior to nanoindentation mapping.

2.5. In depth microstructure analyses

In-depth microstructure analyses were performed using a combination of transmission electron microscopy (TEM), nano-beam diffraction (NBD) strain mapping, transmission Kikuchi diffraction (TKD). For this purpose, two sets of lamellae were prepared from each of the additively manufactured Cantor alloy samples in the as printed and heat-treated states. Lamellae from different regions were prepared using focused ion beam (FIB, ZEISS Crossbeam 340) to entail either columnar or equiaxed grains including their grain boundaries (GBs) in cross-section view.
Analytical TEM was performed subsequently with an FEI Titan Themis 60-300 microscope using high-angle annular dark-field scanning transmission electron microscopy (HAADF-STEM) combined with energy dispersive X-ray spectroscopy (EDS). The microscope was equipped with a high brightness field emission gun (X-FEG), operated at 3.45 kV acceleration voltage and 300 kV extraction voltage, a monochromator, a quadrupole EDS system, an HAADF detector (Fischione Model 3000) and a fast CMOS camera (Ceta, 4k $\times$ 4k).
The effect of annealing time on the strain accumulation at high angle grain boundaries (HAGBs) was studied using the STEM-microprobe mode with a probe size of 1 nm and step sizes below 5 nm in x- and y- directions. Full sets of nanobeam diffraction patterns (NBDPs) were acquired from each sample using drift-corrected spectrum imaging and a custom code written in Digital Micrograph was employed to generate virtual dark-field (DF) images and strain maps extracted from the NBDPs[25,26].
The dislocation density was estimated using orientation maps obtained by TKD from the FIB prepared lamellae and subsequently compared with that of high resolution EBSD maps of the as printed and heat-treated samples in plan parallel view.To obtain local information with comparable resolution, TKD mapping was performed with an identical step size of 0.03 μm for all samples. The dislocation density distribution was obtained using the ATEX software. Fitting the density frequency data was carried out using the Origin software, applying a Rayleigh distribution function.
The local chemistry was analyzed using atom probe tomography (APT) with a local electrode atom probe (LEAP 4000X HR). The samples were thinned down to a needle shape using a ZEISS Auriga 60 FIB. The APT measurements were carried out on samples in the as-prepared and the heat-treated states at temperature set to 60K with a voltage pulse fraction of 20% at a detection rate of 0.5%. The heat-treated sample was annealed at 550°C for 10 h to investigate the grain boundaries and their vicinity.

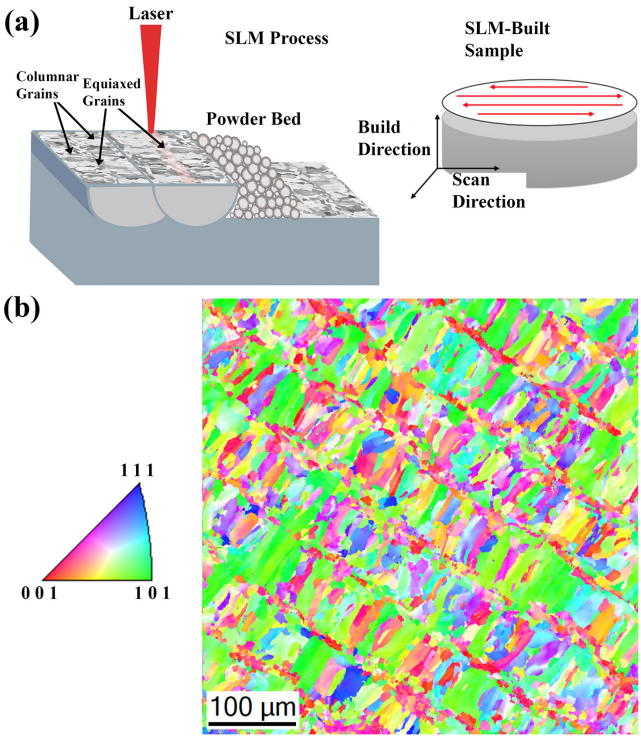

FIG. 1. Synthesis process of the CoCrFeMnNi sample by the SLM method and the final microstructure. (a) An illustration of the synthesis process by the laser irradiation, which results in the formation of a patterned microstructure (left). The final bulk sample which was studied in this report with the specified scan and build directions (right) (c) Resulting microstructure showing equiaxed grains which form under the melt pool and the columnar grains that solidify away from the melt pool.

3. RESULTS

3.1. Initial equiatomic powder

The SEM inspection of the powder particles produced by gas atomization reveals microstructure defects and chemical heterogeneities, dominantly in large particles, see Fig. S1, Supplementary Material. As displayed in Fig. S1(a), particles larger than 45 μm tend to include

pores and feature non-spherical shapes which become more prominent with increased particle size. The porous structure is known to be caused by gas entrapment during the gas atomization process, which influences the true density as well as produces defects in AM materials[27]. The large particles' EDS maps and corresponding line scan profiles are shown in Figs. S1(b) and (c) display the presence of chemical cells enriched in Mn and depleted in Co and Fe, Fig. S1(c, left). Such pores and the heterogeneity of elemental distribution were not observed in the medium-sized particles ranging from 10 to 45 μm, Fig. S1(c, right). Note that only homogeneous and equiatomic medium-sized particles were classified and used for the 3D-printing process of the high-entropy alloy in this study.

3.2. Synthesis of bulk samples

Figure 1(a) illustrates the synthesis process of a bulk CoCrFeMnNi sample. The resulting heterogeneous microstructure is shown by the EBSD inverse pole figure (IPF) orientation map of the as-printed state, Fig. 1(b). The existence of two different grain types, i.e. columnar and equiaxed, results from a space/time heterogeneity of the synthesis (manufacturing) conditions[28]. The equiaxed grains are known to solidify under the melt pool with more isotropic solidification conditions while the laser moves along the predefined track to melt the latest feed of powder particles. The long columnar grains grow epitaxially towards the sides of the melt pool due to high-temperature gradients[28], with one side being connected to the previously processed track and another side in contact with the free space and non-melted powder particles.

3.3. DSC measurements

The results of DSC measurements are presented in Fig. S2, Supplementary Materials. A strong peak with a maximum heat release was observed at about 550°C. In order to elucidate the microstructural changes and defect reactions which are responsible for the heat release, selected samples were subjected to isothermal annealing treatments at 550°C for 1 and 10 h.

3.4. Post annealing hardness maps

Vickers microhardness measurements indicated that the average hardness does not reveal any significant increase after the heat treatment. While the standard deviation decreases with annealing time, the average values remain relatively similar at about 3.26, 3.33 and 3.31 GPa for the as-printed, 1 h annealed as well as 10 h annealed states. High-resolution hardness maps were obtained subsequently by shallow nanoindentations in the as-printed and the heat-treated states. FIB images were acquired from the region of interest (ROI) to provide a better correlation between the hardness map and the underlying microstructure, as shown in Fig. S3. In the as-printed state, the columnar grains show a higher hardness compared to the equiaxed grains, see Fig. S3(a). As a result of the heat treatment, a hardness increase is observed in the columnar grains, see Fig. S3 (b) and Fig. S3(c) which suggests the development of a more homogeneous hardness distribution as the sample is annealed for longer times (10 h) at 550°C.

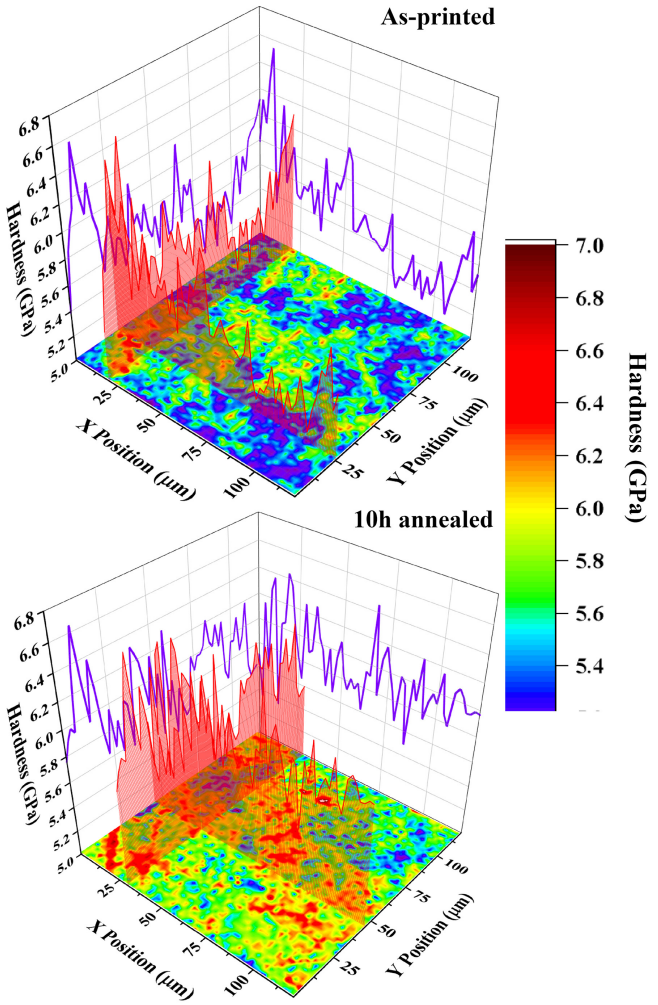

FIG. 2. The high speed – high resolution nanoindentation maps of AM CoCrFeMnNi in the as-printed (upper panel) and the heat-treated (bottom panel) states, showing vertical and horizontal line scan profiles over the hardness maps.

The high speed – high resolution nanoindentation maps of AM CoCrFeMnNi for the as-printed and the heat-treated states are shown in Fig. 2. Especially, the line profiles shown in Figure 2 indicate no significant change for the averaged nano-hardness after prolonged annealing at 550°C for 10 h. However, the hardness distribution is observed to evolve towards homogeneity.

3.5. Element enrichments at high- and low-angle grain boundaries

The STEM HAADF micrographs accompanied by EDS elemental maps in Fig. 3 present a cross-sectional view of the columnar and equiaxed grains along the build direction in the as-printed and heat-treated states. Figure 3 suggests that the AM CoCrFeMnNi alloy has experienced high thermal stress, which manifests as dislocation networks. All samples show an enrichment of Mn and a depletion of Fe and Co at sub-boundaries (dislocation networks) and HAGBs, see Fig. 3. Mn-rich precipitates have also formed inside the matrix in all columnar and equiaxed grains, and their size seems to remain constant even after prolonged heat treatment at 550°C for 10 h. Figures 3 (a) and (b) show a comparison of the microstructures in the as-printed equiaxed and columnar grains. The columnar grains exhibit cellular dislocation networks enriched in Mn with an average cell size of 450 nm which does not change in size and shape after short-term and long-term heat treatments at 550°C, see Figs. 3 (d) and (f). Figure 3 (b) shows Mn-enriched dislocation networks that are elongated along the build direction in the equiaxed grains, which is explained to be due to the upwards thermal gradient during the rapid cooling.

In Fig. 4, bright field (BF) micrographs overlaid by the elemental maps for Mn, Ni, and Cr atoms as well as the corresponding EDS line scan profiles are shown. The as-printed columnar grains in Fig. 4(a) exhibit Mn enrichment at HAGBs together with Cr-rich precipitates which are scarce in numbers and seem to be still in their initial stage of formation. Another observation is that due to different solidification conditions, the boundaries between the columnar grains are more segmented in comparison to the ones between the equiaxed grains. The segments in the HAGBs of the columnar grains are also heterogeneously enriched in Ni, which seems not to be the case for the HAGBs of the equiaxed grains. Further investigations regarding the GB heterogeneity will follow in Fig. 8 and subsection 3.7. After the heat treatment at 550°C for 1 h, an increased enrichment of Cr and Ni at the HAGBs of columnar grains induces a phase separation into Cr-rich and MnNi-rich regions, see Figs. 3(c) and 4(c). However, the equiaxed grains do not exhibit any detectable changes in the distribution of elements due to heat treatment, see Figs. 3 (d) and 4 (d). With a prolonged annealing time of 10 h, Cr enrichment is increasing at the HAGBs of both columnar (Figs. 3 (e) and 4 (e)) and equiaxed (Figs. 3 (f) and 4 (f)) grains.

The co-segregation of Ni and Mn is enhanced after the 10 h annealing at 550°C. Furthermore, the Cr enrichment at HAGBs of columnar grains is accompanied by a pronounced depletion of Ni at the corresponding locations, see Figs. 3 (e) and 4 (e). Figures 3 and 4 substantiate that the phase separation into MnNi- and Cr-rich regions occurs faster (already in the as-printed state, see Fig. 3(c)) and is more pronounced at HAGBs of the columnar grains, whereas it is somewhat retarded at HAGBs of the equiaxed grains.

3.6. Dislocation density and strain maps

The high-resolution EBSD orientation maps and the corresponding Kernel average misorientation (KAM) maps, acquired in the plane-parallel and cross-sectional views, are presented in Fig. 5. The plane-parallel EBSD mapping was carried out on a ROI with an overview of the interface between the columnar and equiaxed grains, see Fig. 5(a). The cross-section orientation maps in Fig. 5(b) were taken in the TKD mode from the electron transparent lamellae which were individually cut from regions with either columnar or equiaxed grains. As suggested by the results in Figs. 5(a) and (b), the misorientation angle between all the grains is higher than 15° and according to Table I there is no considerable change in the dislocation density after 1 h of heat treatment at 550°C either in the plane-parallel or the cross-sectional view. The calculated dislocation density values also remain constant after prolonged annealing up to 10 h.

TABLE I. Dislocation density calculations based on high resolution EBSD and TKD orientation mapping

	as-printed	1 h annealed	10 h annealed
	10^{15} m^{-2}		
HR EBSD	2	3	3
TKD columnar grain	0.3	1	2
TKD equiaxed grain	2	1	1

To map the local elastic strains, a full set of NBED patterns at each probe position was acquired. Figure 6 shows the virtual dark field images along with the corresponding *elastic* strain maps nearby a high-angle GB in the region of equiaxed grains for the as-printed and heat-treated states. The rotational and hydrostatic (dilation/compression) components of the elastic strain tensor were determined, analyzing the shifts in the diffraction spots[26] with respect to a reference position. The shear component map shows no significant change between the as-printed and heat-treated states and is, for this reason, not shown in this figure. The grain average has been used as reference for the elastic strain. Moreover, it is worth noting that the reported strains are well above the accuracy of this technique, which was estimated to be about 0.1% for the custom-built code[26,29]. Similar method has also been used in literature to yield results of high accuracy in terms of strain distribution with nm-scale resolution[30,31]. The virtual dark field (DF) image, hydrostatic component and rotational strain maps are reconstructed from a set of diffraction patterns using the custom-built code written as a plug-in for digital micrograph[25,26]. In Fig. 6, overlays of STEM DF micrographs together with the Mn, Ni, and Cr elemental maps are additionally shown to provide a better understanding of the interaction between the segregation at HAGBs and

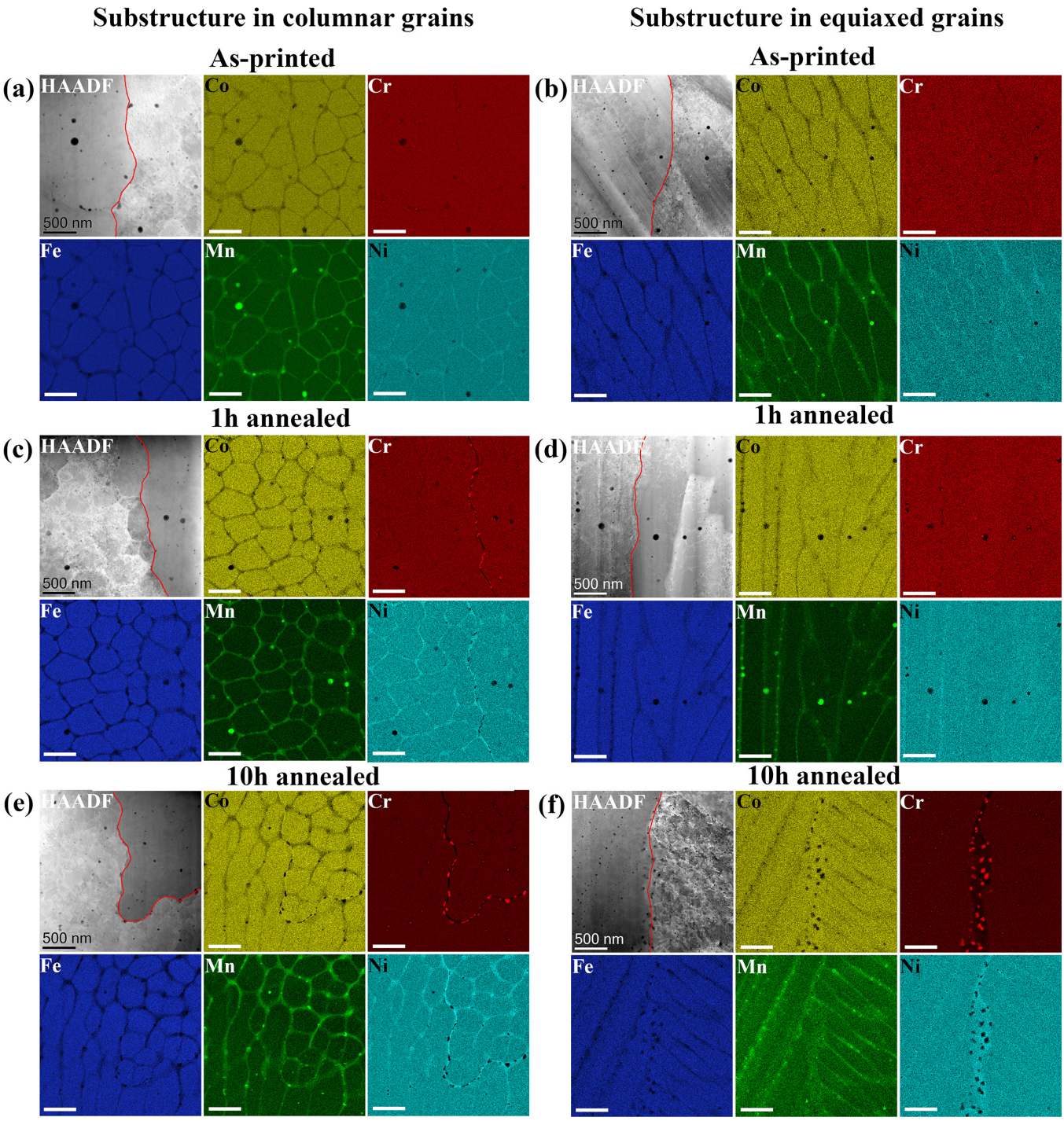

FIG. 3. STEM HAADF micrographs and elemental maps of the additively manufactured CoCrFeMnNi alloy in the as-printed state (a and b), 1 h annealed at 550°C (c and d) and 10 h annealed at 550°C (e and f). The cross-sectional view of the columnar grains and the GBs between them indicated by the red line (a, c and d) displayed next to the equiaxed grains and their GBs indicated by the red line (b, d and f) for all states provides an overview of the microstructure in different grain types as a function of annealing time. All scale bars in STEM elemental maps correspond to 500 nm.

the strain fields. It is worth noting that STEM micrographs and EDS overlays are now linked with nanobeam diffraction patterns to identify each phase and its orientation. According to Fig. 6 (b) the Mn-rich precipitate has grown inside the matrix having the same FCC structure as the grain. The Cr-rich phase which forms after 1h at 550°C in the vicinity of the Mn-rich precipitate is identified as the sigma phase. Both Mn-rich precipitate

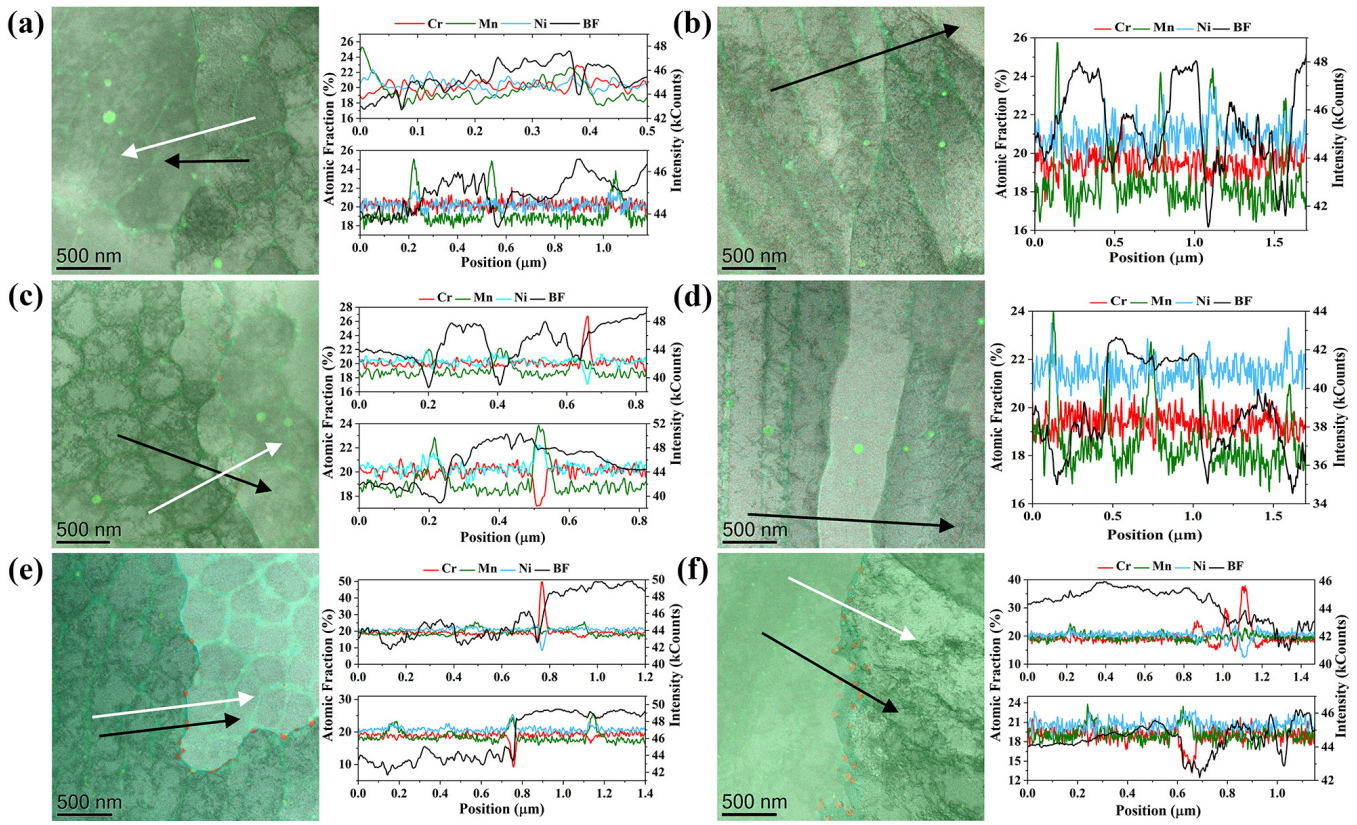

FIG. 4. STEM BF micrographs with Mn, Ni, and Cr elemental maps overlay and the corresponding EDS line scan profiles for columnar (a, c, e) and equiaxed (b, d, f) grains. The as-printed state shows relatively similar Mn enrichment at HAGBs and in dislocation networks of equiaxed (a) and columnar (b) grains. After 1 h of annealing at 550°C, phase separation into MnNi-enriched (white arrow, upper panel) and Cr-enriched regions (black arrow, low panel) starts at the HAGBs of the columnar grains (c), but the segregation levels of elements to HAGBs and dislocation networks are not significantly changed at the equiaxed grains (d). Prolonged annealing at 550°C for 10 h results in pronounced separation of MnNi- (white arrow, low panel) and Cr-enriched (black arrow, upper panel) phases at the HAGBs of the columnar grains (e) and development of Cr-rich precipitates (black arrow, upper panel) within MnNi-enriched regions (white arrow, low panel) at the HAGBs of the equiaxed grains (f).

and Cr-rich phase, which cause dislocation pile-ups in the neighboring regions, and have the same [001] orientation as the grain. Fig. 6 (c) shows that after 10 h of annealing at 550°C the Cr-rich sigma phase has grown at the HAGBs. The Cr-rich sigma phase also formed in the same orientation as the main grain along the [113] direction, leading to compressive strain in the matrix, as shown by the hydrostatic component map in Fig. 6 (c).

The intensity of rotational strain increases from 0.3° to 0.8° after 10 h of annealing at 550°C. This together with the STEM DF micrographs and the elemental map overlay is evidence to two concurrent processes. Cr segregation to GB segments with nearly equiatomic composition (initially segregation-free segments), and minimization of local stresses (including those induced by local atom transport) followed by dislocation rearrangements which are blocked at the GB, especially after enhanced segregation. Thus, the two processes would result in enhanced segregation and enhanced residual stress at the GB. The enhanced Cr precipitation and phase separation towards Cr-rich and MnNi-rich phases give rise to higher stresses and to dislocation accumulation at the GB, respectively, shown by the rotational and hydrostatic component maps in Fig. 6 (c).

3.7. Phase separation at HAGBs

The results of an APT analysis conducted on needles prepared from the samples in as-printed and heat-treated (at 550°C for 10 h) states are shown in Fig. 7. The mass spectrum used for identification of the elements is presented in the supplementary materials [See Fig. S4]. A homogeneous distribution of the alloying elements is found in the as-printed CoCrFeMnNi for an APT needle cut from a region inside the grain bulk, Fig. 7(a). The chemical composition of the needle in the as-printed state agrees with the equiatomic CoCrFeMnNi and the detected amounts of carbon or oxygen are below 1 at.%. After 10 h heat treatment, the reconstructed needle exhibits a heteroge-

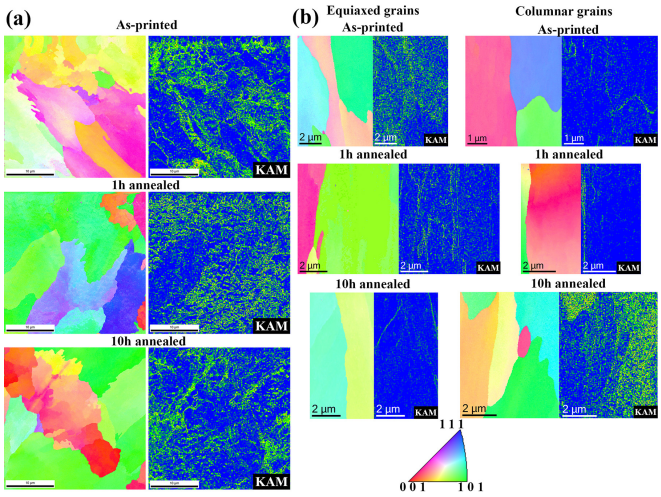

FIG. 5. High resolution electron back-scatter diffraction (EBSD) orientation maps and the kernel average misorientation (KAM) maps in the as-printed and heat treated states. The estimated dislocation densities change not significantly after annealing treatments at 550°C for 1 h and 10 h. (a) High resolution maps taken in the plane-parallel view from a ROI with a mixture of columnar and equiaxed grains. (b) Cross-section view EBSD and KAM maps taken in transmission kikuchi diffraction (TKD) mode from lamellae prepared from the region of interest using the focused ion beam (FIB) technique.

neous microstructure, segregation of the elements to the GB, and indicates a phase decomposition, see Fig. 7(b). The iso-concentration surfaces for the heat-treated sample drawn for Ni = 30 at.% and Cr = 30 at.% show a strong segregation of elements and phase separation at the GB, Fig. 7(c). An almost equiatomic composition is found in the grain interior, while Ni, Fe and Co are enriched in the vicinity of the GB and show a drop in concentration at the GB location where the Cr-rich sigma phase develops. The phase separation at the GB into Ni-rich and Cr-rich regions in Fig. 7(c) is in agreement with the findings in Fig. 6(c) and Fig. 4(f).

3.8. Segregation and phase separation at HAGBs

In Fig. 8, bright-field micrographs of HAGBs in the columnar and equiaxed grain areas are shown for different states with STEM EDS map overlays and the corresponding line scan profiles. In the as-printed state, the high-angle GBs in both columnar and equiaxed grains are found to exhibit a strongly heterogeneous Ni enrichment, enhanced probably at certain GB segments or GB areas. It might be speculated that these GB areas consist of a high local density of defects, as e.g. GB dislocations and/or disconnections, Fig. 8(a). Note that an impact of GB disconnections on kinetic[32] and thermodynamic[33] properties of GBs has been reported already. However, due to the complexities concerning direct – atomically

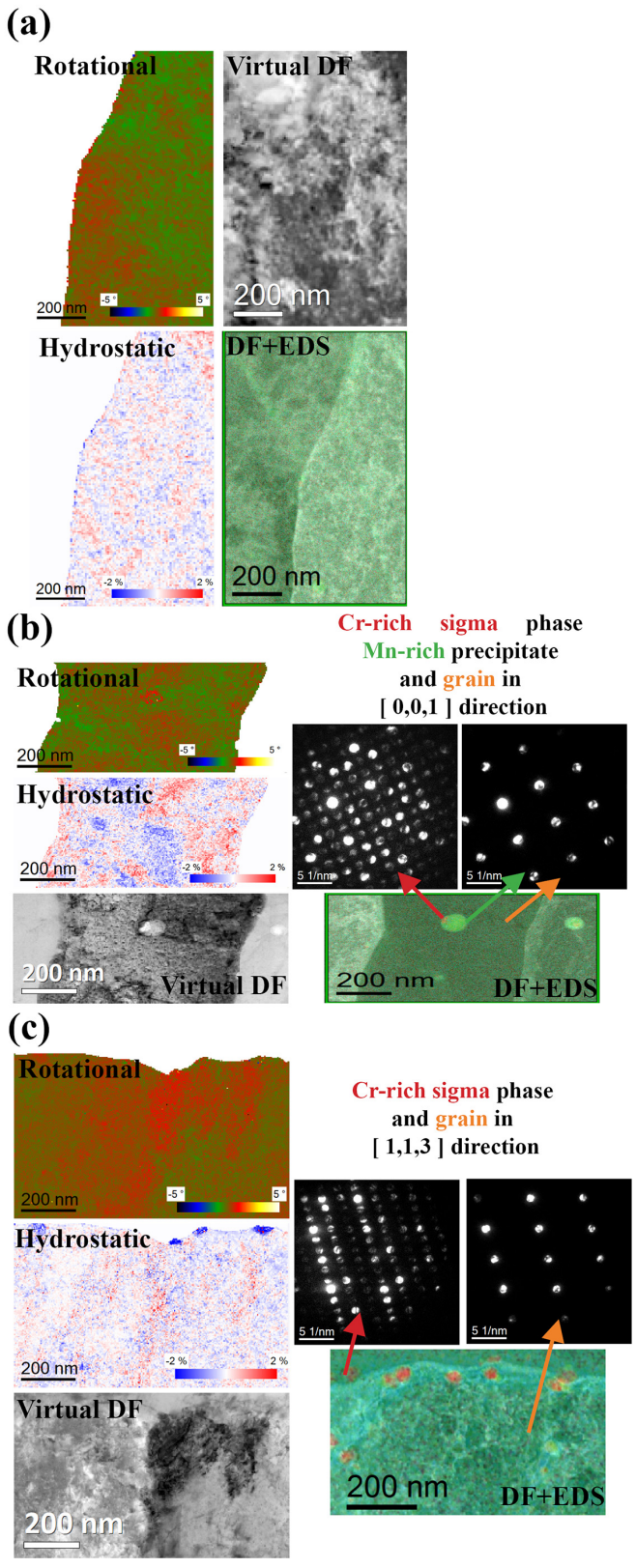

FIG. 6. Reconstructed virtual-dark field image and the corresponding maps representing rotational and hydrostatic components of the elastic strain tensors together with the STEM DF micrographs and the Mn, Ni and Cr elemental map overlay and the corresponding diffraction patterns for different states: (a) as-printed, (b) 1 h annealed and (c)10 h annealed.

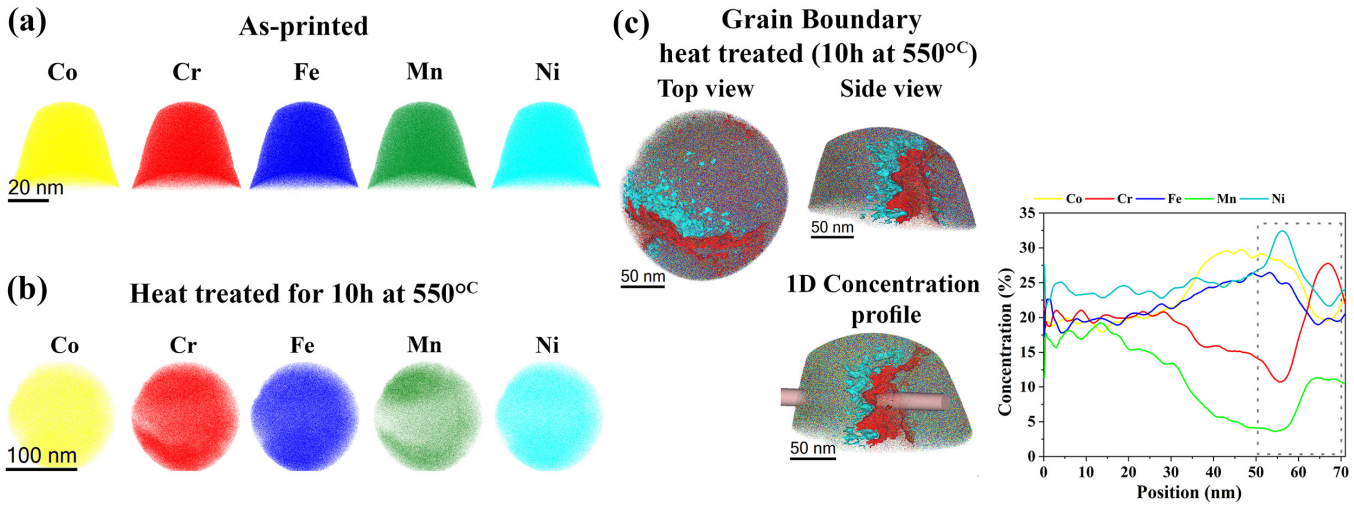

FIG. 7. 3D reconstructed needles in the as-printed (a) and heat-treated (b-c) states. The as-printed sample reveals a homogeneous elemental distribution in the matrix between the dislocation walls (a). Increased heterogeneity in the local chemistry close to the HAGB after 10 h of annealing at 550°C (b). Iso-surface maps of the heat-treated sample with Ni (30 at.%) in cyan and Cr (30 at.%) in red, along with the respective concentration profile from the cylindrical ROI (c).

resolved – imaging of such defects at a GB, particularly when complex alloy chemistry is also involved, direct evidence for the presence of such defects requires a separate study. The heterogeneity of the GB enrichment tends to be more pronounced in the columnar grains in both as-printed and heat-treated states, compare Figs. 3 and 4. After annealing at 550°C for 1 h, no significant changes are recorded for the HAGBs of equiaxed grains with respect to the as-printed state, whereas the HAGBs of the columnar grains reveal Cr nano-precipitation at HAGBs and a preferential enrichment of either Ni or Cr at different GB segments (regions), see Figs. 3 and 4. Furthermore, the line scan profile in Fig. 8(b) suggests that the phase decomposition into Ni- and Cr-rich regions has occurred at some GB segments of the columnar grain. As shown in Fig. 8(c) this phase separation becomes more prominent after longer annealing time for 10 h and is observed in both equiaxed and columnar grain types. The interplay between the Cr- and Ni-enrichments along and across the HAGB is shown in Fig. 8(c) for both columnar and equiaxed grains. The decomposition towards the formation of alternating Ni/Cr-enriched nano-scale regions along the same GB resembles a spinodal-like GB transformation, as observed in CoCrFeMnNi[34] and Fe-Mn-Cr alloys[35].

The GB excess number of atoms of the ith element, Γ_i, is formally defined as,

$$\Gamma_{\mathrm{i}} = \frac{\mathrm{N_i^{gb}} - \mathrm{N_i^{eq}}}{A}. \tag{1}$$

Here $\mathrm{N_i^{eq}}$ represents the number of ith atoms present in the volume with no segregation, $\mathrm{N_i^{gb}}$ is the number of atoms present in the same volume with segregation, and A is the cross-section area of the volume. By definition, the value of Γ_i in Eq. (1) provides a GB excess *averaged* over the reference GB area A. Using the STEM EDS line scans, one may quantify the *local* values of the GB excess.

The difference of the numbers $\mathrm{N_i^{eq}}$ and $\mathrm{N_i^{gb}}$ is determined by integrating the real element distribution with respect to the one without segregation,

$$\mathrm{N_i^{gb}} - \mathrm{N_i^{eq}} = \frac{\mathrm{N_t}}{L} \int_0^{\mathrm{L}} \left(\mathrm{X_i^{gb}} - \mathrm{X_i^{eq}} \right) dx. \tag{2}$$

Here $\mathrm{N_t}$ is the total number of atoms in the sampling volume, L is the length of the line scan, and $\mathrm{X_i}$ is the atomic fraction of the ith element measured using STEM EDS line scans in the presence of segregation ($\mathrm{X_i^{gb}}$) or in the absence of it ($\mathrm{X_i^{eq}}$). In the present work, the $\mathrm{X_i^{eq}}$ values are averaged over the grain interiors and artificially prolonged across the GBs mimicking a segregation-free state.

In the case of a line scan, the effective cross-section area, A, of the reference volume is simply $A = \Omega/L$, where Ω is the atomic volume of the alloy. Finally, the GB excess is found as,

$$\Gamma_i = \frac{N_t}{\Omega} \int_0^{L} \left(X_i^{\mathrm{gb}} - X_i^{\mathrm{eq}} \right) dx. \tag{3}$$

Taking into account the integral analysis of the STEM EDS data, the local GB excess values are averaged over the area determined by the foil thickness (about 80 to 90 nm) and the effective size of the excited volume (about 40 nm).

In Table II, the determined GB excesses of Cr and Ni at HAGBs in columnar and equiaxed grain areas are listed as a function of annealing time for several representative positions. The dispersion of the determined GB excesses

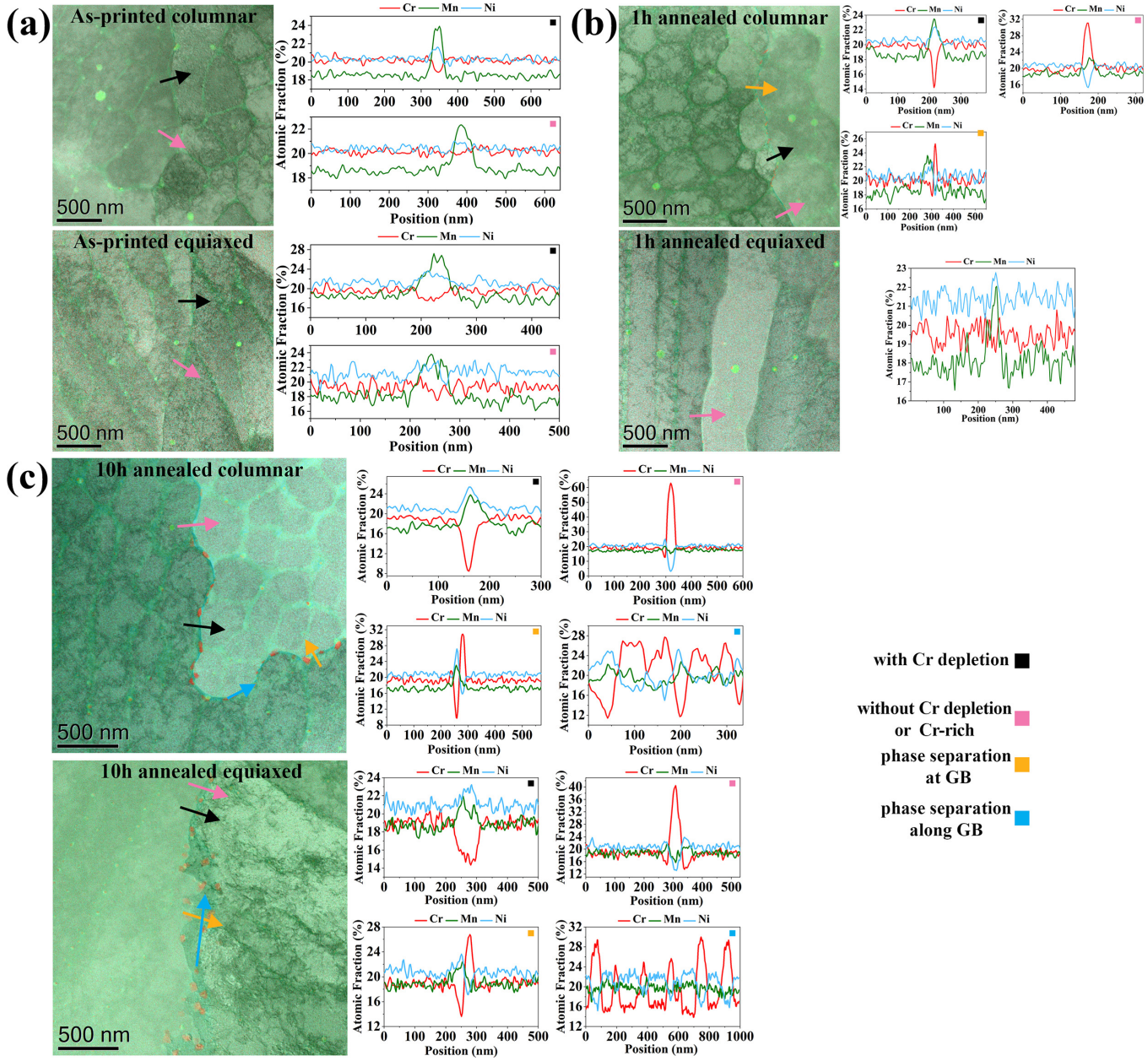

FIG. 8. BF micrographs with STEM EDS elemental map overlay and line scan profiles showing the compositional heterogeneity at HAGBs as a function of annealing time. The black and pink arrows show the GB segments with and without a Cr depletion. The phase separation across and along the GB is indicated by the orange and blue arrows in that order. (a) Preferential enrichment of Ni in the GB segments of columnar and equiaxed grains. (b) Start of precipitation and spinodal-like phase decomposition after 1 h of annealing at 550°C in the GB segments of columnar grain while the equiaxed grain shows no considerable change. (c) Comparable trends of phase separation in the columnar and equiaxed grains after 10 h of heat treatment at 550°C. The color of the symbols in upper-right corner of line scan plots corresponds to the arrows in the BF micrographs.

characterizes the heterogeneity of the segregation in each particular state, Table II.

Fig. 8 substantiates the strong heterogeneity of chemical composition at HAGBs in the as-printed columnar and equiaxed grains. A preferential enrichment of Ni to certain GB segments is detected in the as-printed state, Fig. 8(a), which is enhanced after 1 h of annealing at 550°C. Variable states of elemental enrichment and phase separation are observed in the columnar grain, while the equiaxed grain remains similar to its as-printed state, Table II and Fig. 8 (b). After 10 h of annealing at 550°C, the columnar and equiaxed grains follow the same trends in the variation of GB excess values for Cr and Ni. The phase decomposition presented in Figs. 8(b) and (c)

TABLE II. GB excesses, Γ, of Cr and Ni determined at several representative segments of HAGBs within columnar and equiaxed grain regions in the as-printed and heat-treated states using the STEM EDS line scans. An absence of the (reference area-averaged) element enrichment with a simultaneous phase separation along the HAGB is indicated by the superscript *. The GB excess values have an uncertainty of 10% which originates from the STEM EDS line scans.

Annealing time (h)	Type of grains	Pos.#1		Pos.#2		Pos.#3	
		Γ_{Cr}	Γ_{Ni}	Γ_{Cr}	Γ_{Ni}	Γ_{Cr}	Γ_{Ni}
		(atoms/nm^2)					
0	Columnar	0	0	-28	27	-43	75
	Equiaxed	0	0	-74	87	0	0
1	Columnar	-77	38	206	-80	0*	0*
	Equiaxed	0	18	0	0	0	0
10	Columnar	-219	112	1040	-378	0*	0*
	Equiaxed	-242	85	519	-197	0*	0*

agrees with the alternating fluctuations of Γ_{Ni} and Γ_{Cr} in Table II. This phase separation mechanism in columnar and equiaxed grains enables to keep the balance between the elements with the highest likelihood of diffusing into HAGBs after heat treatment.

4. DISCUSSION

The collective results are indicative of the microstructure evolution from the as printed state after synthesis to a more homogeneous state after heat treatment involving complex mechano-chemical phenomena such as heterogeneous segregation, nano-precipitation and phase separation. STEM EDS line scans in Figs. 4 (a) and (b) show similar atomic percentages for the Mn enrichment at high- and low-angle GBs in the as-printed equiaxed and columnar grains, which is consistent with the findings of recent studies[22]. We may speculate that the Mn entrapment in the dislocation networks or HAGBs is likely to trace back to the synthesis process, where Mn is preferentially evaporated and diffuses back into the solidifying grains from the gas phase through the short-circuit diffusion paths. The co-segregation of Mn and Ni at the HAGBs in Fig. 4 is probably facilitated by Ni diffusion in the solidified grains and thermodynamically triggered by the attractive Ni-Mn interaction with the formation of a new ($L1_0$-ordered NiMn) phase[36].

The segmented HAGBs in the columnar grains are an indicator of a higher GB energy in comparison to the equiaxed grains with relatively straight GBs, see Fig. 3. The formation of microstructure at the growing solid-liquid interface is determined by the degree of constitutional undercooling which satisfies the continuity of matter and heat equations through different solidification modes[37]. The most important parameters that govern the solidification of an alloy are the thermal gradient (G) and the solidification rate (R)[38]. The thermal gradient is given in our case by the temperature field generated by the laser source. The solidification rate is related to the beam velocity and the shape of the melt pool. During the SLM process, the solid acts as a heat sink and solidification is mostly directional, whereas the heat flow is opposite to the growth direction[39]. The change in concentration in front of the solid-liquid interface will affect the local equilibrium solidification temperature. As a result, the interface structure varies from a planar to a cellular structure when conditions get close to absolute stability[38,40]. Thus, the volume fraction of equiaxed grains is high at regions with low G/R ratios, whereas higher G/R ratios give rise to the formation of columnar grains[41]. Since the columnar grains form in zones which feature higher thermal gradients and lower solidification rates, this also results in a higher density of defects in comparison with the equiaxed grains[20].

Due to locally different energy states (anisotropy of GB energy and GB tension[42–44], the presence of disconnection defects[33], etc.), certain segments of the as-printed columnar grains exhibit Ni enrichment while others retain an equiatomic composition as shown in Fig. 8(a). The segments with higher Ni concentrations reveal higher stability by preventing phase decomposition or formation of Cr-rich precipitates. However, regions with equiatomic composition or even Ni depletion promote the formation of the Cr-rich sigma phase. These findings are in line with the formation of Cr-rich sigma phase in a CoCrFeMnNi alloy reported by Laplanche[45]. Moreover, after 1 h of annealing at 550°C, the initially segregation-free (equiatomic) segments are found to develop towards a Cr-enriched state, whereas the Ni-rich segments remain relatively unaffected (see Figs. 4(c) and 8(b) and Table II). Bracq et al.[46] identified Cr and Mn as elements which destabilize the fcc solid solution in CoCrFeMnNi HEA. According to our observation, the Cr increase triggers the phase separation at HAGBs, which are preferential nucleation sites for the formation of the Cr-rich sigma phase[45]. In addition, prolonged annealing leads to Cr saturation at dislocations, also favoring nucleation of the Cr-rich sigma phase in the grain interiors.

The kinetics of phase decomposition is affected by de-

fects present in the as-manufactured state[47]. Thus, the different kinetics of phase decomposition in equiaxed and columnar grains indicate different densities of residual defects, which are probably point defects and dislocations. It is worth noting that the 10 h heat treatment at 550°C was long enough to trigger a pronounced phase separation in both equiaxed and columnar grains. According to the strain maps in Fig. 6 the rotational strain increases from 0.3° in the as-printed state to 0.7°. The dislocations and their corresponding strain fields as displayed in the reconstructed virtual DF image in Fig. 6 show an overlap of shear, dilatation and rotational strains for all states. This is indicative of a complex microstructure in the vicinity of the GBs. The presence of elevated elastic strain at GB segments with Cr enrichment, followed by phase decomposition into adjacent Cr-rich and MnNi-rich GB areas, indicates a complex mechanochemical coupling phenomenon. This would then govern the GB transformation[48] and probably favor the role of GB defects, such as disconnections[33], in this fundamental process.

To provide further information on the mechanism responsible for the formation of Cr-rich precipitates at HAGBs and in the grain interiors, we have used the initial powder, similar to that characterised in Fig. S1, Supplementary material, to produce a solid disk using a mechanical alloying technique via high-pressure torsion (HPT). The microstructure analysis of the HPT-produced sample reveals that Cr-rich precipitate have formed and grown in size after one ho of annealing at 425°C (see Fig. S5(c)). The formation of Cr-rich precipitates has been reported to start after a few minutes at temperatures above 450°C due to conditions provided by the severe plastic deformation that accelerate the phase decomposition processes[47]. Although Mn is the fastest diffusing element in the CoCrFeMnNi HEA[49] and features the lowest barrier for atom–vacancy jumps[50], above 500°C the formation of the Cr-rich precipitates in equiatomic CoCrFeMnNi is favored thermodynamically[9]. However, formation of MnNi-rich precipitates becomes more favorable at lower temperatures[951], which correlates with enhanced Mn (and Ni) segregation in the HPT-processed powder, see Fig. S5(b). Enhanced concentrations of vacancies (processing-induced/ non-equilibrium), enhance atomic mobility and favor Mn segregation to the dislocation networks of the SLM-built Cantor alloy, see Fig. 4. The defect-solute complexes have been considered[52] as precursors for Cr-rich precipitate formation that turns the vacancy clusters into nuclei for Cr segregation[52]. Since one of the main differences between the CoCrFeMnNi alloys prepared by the HPT and AM methods is the density of defects and of so-called 'non-equilibrium' GBs (the 'non-equilibrium' state of high-angle GBs in 3D-printed CoCrFeMnNi alloy has been discovered by Choi et al.[24]), these defects could be identified as one of the major factors that trigger the Cr-precipitation and/or reduce its onset temperature.

Furthermore, the residual amount of synthesis-induced defects seems to trigger the Cr precipitation in columnar grains and the postponed phase decomposition in equiaxed grains correlates with a decreased concentration of excess (quenched-in) vacancies after the same treatment conditions, Fig. 3.

The high resolution hardness maps in Fig. 2 characterize the equiaxed grains as being softer compared to the columnar grains in the as-printed state. This originates from the fact that the Mn-enriched cellular dislocation networks in the columnar grains contribute more to the pinning of dislocations than the Mn-enriched shear bands in the equiaxed grains, which are mostly oriented along the build direction, see Fig. 3. Finally, the APT results in Fig. 7 together with the strain maps in Fig. 6 show that the increased chemical heterogeneity and localized nano-precipitation in the matrix together with the enrichment of elements at dislocation networks and phase separation at HAGBs give rise to the increased hardness in the material. Furthermore, since columnar grains have a higher energy, the propensity for forming new phases or developing new chemical compounds is there even higher, which in turn contributes to the enhanced mechanical properties of such grains.

5. SUMMARY AND CONCLUSIONS

The unique microstructure of an additively manufactured and annealed CoCrFeMnNi alloy was the focus of this study, starting at the surface with high-resolution nanoindentation hardness maps, and finishing with the local analyses of the nanosized reinforcing phases as well as strain distributions at the HAGBs. Our in-depth analysis covers different aspects; that is a complex mechanochemical coupling manifested by anisotropic segregation and GB phase separation. The collective effect of different strengthening mechanisms in this SLM-produced FCC HEA system makes the manipulation and fine-tuning of the materials' properties feasible, and thus paves the way for further applications.

The main findings of this study are:

- The Mn segregation to high-angle GBs and dislocation walls in the as-printed state is probably induced by its laser-assisted evaporation during the synthesis and subsequent rapid diffusion from the gas phase into the alloy. This could have occurred after crystallization along the formed dislocation and GB networks, i.e., the short-circuit paths. The observed similar enrichment of Mn atoms at low- and high-angle GBs in the fabricated alloy are explained by kinetic trapping and attributed to the highly non-equilibrium conditions of the material preparation.

- Chemical interaction of Ni and Mn favors Ni enrichment at low-angle and high-angle grain boundaries. This enrichment is observed to be non-homogeneous along interfaces in a way,

that off-equiatomic (with segregation) and nearly equiatomic (no segregation) areas were found for different segments of high-angle grain boundaries in the as-printed state. This leads to phase separation after 10 h heat treatment at 550°C which manifests itself as Cr-rich and MnNi-rich regions in the HAGBs of both columnar and equiaxed grains.

- The Cr-rich (σ-) phase nucleates at the HAGBs between the columnar grains and in the vicinity of Mn-rich precipitates. Formation of Cr–vacancy pairs (due to an increased concentration of preparation-induced and quenched vacancies) in the columnar grains lowers the kinetic barrier that triggers the growth of Cr-rich precipitates. The precipitates grow on one side of the grain boundary during annealing and exert strain onto the grain.

- The as-printed alloy reveals a high dislocation density of about $2.5 \cdot 10^{15}$ m^{-2} due to high thermal stresses and a local heterogeneity in the elemental distribution during processing. Despite the unaffected dislocation density which remains relatively similar after annealing at 550°C for 1 h and 10 h, the measured local strains do not relax. Moreover, the rotational strains even increase after 10 h of annealing at 550°C, especially in the vicinity of the HAGBs that is explained by nucleation and growth of Cr-rich and Ni-rich phases and nano-precipitates.

- The anisotropy of the GB surface tension gives rise to an enhanced heterogeneity of element enrichment at grain boundaries, with certain GB segments being enriched in Mn and Ni and others enriched in Cr. These findings highlight the complexity of mechano-chemical coupling in additive manufacturing of HEAs triggered by annealing.

ACKNOWLEDGEMENT

The authors would like to thank Mr. Manoel W. da Silva Pinto for his support with DSC measurements. Financial support from Deutsche Forschungsgemeinschaft (DFG) via research grants (DI 1419/19-1 and WI1899/32-2) is acknowledged.

[1] J.W. Yeh, S.K. Chen, S.J. Lin, J.Y. Gan, T.S. Chin, T.T. Shun, C.H. Tsau, and S.Y. Chang. Nanostructured high-entropy alloys with multiple principal elements: novel alloy design concepts and outcomes. *Advanced Engineering Materials*, 6(5):299–303, 2004.

[2] Yong Zhang, Ting Ting Zuo, Zhi Tang, Michael C. Gao, Karin A. Dahmen, Peter K. Liaw, and Zhao Ping Lu. Microstructures and properties of high-entropy alloys. *Progress in Materials Science*, 61(September 2013):1–93, 2014.

[3] C. Y. Yap, C. K. Chua, Z. L. Dong, Z. H. Liu, D. Q. Zhang, L. E. Loh, and S. L. Sing. Review of selective laser melting: Materials and applications. *Applied Physics Reviews*, 2(4), 2015.

[4] Mohit Dharnidharka, Utkarsh Chadha, Lohitha Manya Dasari, Aarunya Paliwal, Yash Surya, and Senthil Kumaran Selvaraj. Optical tomography in additive manufacturing: a review, processes, open problems, and new opportunities. *European Physical Journal Plus*, 136(11), 2021.

[5] Stéphane Gorsse, Christopher Hutchinson, Mohamed Gouné, and Rajarshi Banerjee. Additive manufacturing of metals: a brief review of the characteristic microstructures and properties of steels, Ti-6Al-4V and high-entropy alloys. *Science and Technology of Advanced Materials*, 18(1):584–610, 2017.

[6] Chen Zhang, Junkai Zhu, Huai Zheng, Hui Li, Sheng Liu, and Gary J. Cheng. A review on microstructures and properties of high entropy alloys manufactured by selective laser melting. *International Journal of Extreme Manufacturing*, 2(3), 2020.

[7] B. Cantor. Multicomponent high-entropy cantor alloys. *Progress in Materials Science*, 120:100754, 2021.

[8] B. Cantor, I.T.H. Chang, P. Knight, and A.J.B. Vincent. Microstructural development in equiatomic multicomponent alloys. *Materials Science and Engineering: A*, 375-377(1-2 SPEC. ISS.):213–218, jul 2004.

[9] F. Otto, A. Dlouhý, Ch Somsen, H. Bei, G. Eggeler, and E. P. George. The influences of temperature and microstructure on the tensile properties of a CoCrFeMnNi high-entropy alloy. *Acta Materialia*, 61(15):5743–5755, 2013.

[10] Y.-K. Kim, S. Yang, and K.-A. Lee. Superior Temperature-Dependent Mechanical Properties and Deformation Behavior of Equiatomic CoCrFeMnNi High-Entropy Alloy Additively Manufactured by Selective Laser Melting. *Scientific Reports*, 10:18006, 10 2020.

[11] N. Eißmann, U. Mühle, U. Gaitzsch, G. Walther, T. Weißgärber, and B. Kieback. Precipitation hardening of high entropy alloy CoCrFeMnNi containing titanium. *Journal of Alloys and Compounds*, 857:157610, 2021.

[12] Ruidi Li, Pengda Niu, Tiechui Yuan, Peng Cao, Chao Chen, and Kechao Zhou. Selective laser melting of an equiatomic CoCrFeMnNi high-entropy alloy: Processability, non-equilibrium microstructure and mechanical property. *Journal of Alloys and Compounds*, 746:125–134, 2018.

[13] Y. Chew, G. J. Bi, Z. G. Zhu, F. L. Ng, F. Weng, S. B. Liu, S. M.L. Nai, and B. Y. Lee. Microstructure and enhanced strength of laser aided additive manufactured CoCrFeNiMn high entropy alloy. *Materials Science and Engineering A*, 744(October 2020):137–144, 2019.

[14] Y.-K. Kim, S. Yang, and K.-A. Lee. Compressive creep behavior of selective laser melted CoCrFeMnNi high-entropy alloy strengthened by in-situ formation of nano-oxides. *Additive Manufacturing*, 36:101543, 2020.

[15] Y.-K. Kim, M.-S. Baek, S. Yang, and K.-A. Lee. In-situ formed oxide enables extraordinary high-cycle fatigue

resistance in additively manufactured CoCrFeMnNi high-entropy alloy. *Additive Manufacturing*, 38:101832, 2021.

[16] Bowen Wang, Miao Sun, Bobo Li, Lijuan Zhang, and Bingheng Lu. Anisotropic response of cocrfemnni high-entropy alloy fabricated by selective laser melting. *Materials*, 13(24):1–17, 2020.

[17] Young Kyun Kim, Jungho Choe, and Kee Ahn Lee. Selective laser melted equiatomic CoCrFeMnNi high-entropy alloy: Microstructure, anisotropic mechanical response, and multiple strengthening mechanism. *Journal of Alloys and Compounds*, 805:680–691, 2019.

[18] Christian Haase, Florian Tang, Markus B. Wilms, Andreas Weisheit, and Bengt Hallstedt. Combining thermodynamic modeling and 3D printing of elemental powder blends for high-throughput investigation of high-entropy alloys – Towards rapid alloy screening and design. *Materials Science and Engineering A*, 688(January):180–189, 2017.

[19] Jeong Min Park, Jungho Choe, Jung Gi Kim, Jae Wung Bae, Jongun Moon, Sangsun Yang, Kyung Tae Kim, Ji Hun Yu, and Hyoung Seop Kim. Superior tensile properties of 1additively manufactured by selective laser melting. *Materials Research Letters*, 8(1):1–7, 2020.

[20] Hongge Li, Yongjiang Huang, Songshan Jiang, Yunzhuo Lu, Xiaoyu Gao, Xing Lu, Zhiliang Ning, and Jianfei Sun. Columnar to equiaxed transition in additively manufactured CoCrFeMnNi high entropy alloy. *Materials and Design*, 197:109262, 2021.

[21] Z. G. Zhu, Q. B. Nguyen, F. L. Ng, X. H. An, X. Z. Liao, P. K. Liaw, S. M.L. Nai, and J. Wei. Hierarchical microstructure and strengthening mechanisms of a CoCrFeNiMn high entropy alloy additively manufactured by selective laser melting. *Scripta Materialia*, 154(May):20–24, 2018.

[22] Yi Ting Lin, Xianghai An, Zhiguang Zhu, Mui Ling Sharon Nai, Che Wei Tsai, and Hung Wei Yen. Effect of cell wall on hydrogen response in CoCrFeMnNi high-entropy alloy additively manufactured by selective laser melting. *Journal of Alloys and Compounds*, 925:166735, 2022.

[23] E. J. Pickering, R. Muñoz-Moreno, H. J. Stone, and N. G. Jones. Precipitation in the equiatomic high-entropy alloy CrMnFeCoNi. *Scripta Materialia*, 113:106–109, 2016.

[24] Nuri Choi, Vladislav Kulitckii, Josua Kottke, Bengü Tas, Jungho Choe, Ji Hun Yu, Sangsun Yang, Joo Hyun Park, Jai Sung Lee, Gerhard Wilde, and Sergiy V. Divinski. Analyzing the 'non-equilibrium state' of grain boundaries in additively manufactured high-entropy cocrfemnni alloy using tracer diffusion measurements. *Journal of Alloys and Compounds*, 844:155757, 2020.

[25] Christoph Gammer, V. Burak Ozdol, Christian H. Liebscher, and Andrew M. Minor. Diffraction contrast imaging using virtual apertures. *Ultramicroscopy*, 155:1–10, aug 2015.

[26] V. B. Ozdol, C. Gammer, X. G. Jin, P. Ercius, C. Ophus, J. Ciston, and A. M. Minor. Strain mapping at nanometer resolution using advanced nano-beam electron diffraction. *Applied Physics Letters*, 106(25), jun 2015.

[27] Pan Wang, Pengfei Huang, Fern Lan Ng, Wai Jack Sin, Shenglu Lu, Mui Ling Sharon Nai, Zhi Li Dong, and Jun Wei. Additively manufactured CoCrFeNiMn high-entropy alloy via pre-alloyed powder. *Materials and Design*, 168:107576, 2019.

[28] Alexander F. Chadwick and Peter W. Voorhees. The development of grain structure during additive manufacturing. *Acta Materialia*, 211:116862, jun 2021.

[29] C. Gammer, J. Kacher, C. Czarnik, O. L. Warren, J. Ciston, and A. M. Minor. Local and transient nanoscale strain mapping during in situ deformation. *Applied Physics Letters*, 109(8), 2016.

[30] K. Müller, A. Rosenauer, M. Schowalter, J. Zweck, R. Fritz, and K. Volz. Strain Measurement in Semiconductor Heterostructures by Scanning Transmission Electron Microscopy. *Microscopy and Microanalysis*, 18:995–1009, 2012.

[31] D. Cooper, T. Denneulin, J. P. Barnes, J. M. Hartmann, L. Hutin, C. Le Royer, A. Béché, and J. L. Rouvière. Strain mapping with nm-scale resolution for the silicon-on-insulator generation of semiconductor devices by advanced electron microscopy. *Journal of Applied Physics*, 112(12), 2012.

[32] L. Zhang, J. Han, D.J. Srolovitz, and Y. Xiang. Equation of motion for grain boundaries in polycrystals. *npj Comput Mater*, 7:64, 2021.

[33] Chongze Hu, Douglas L. Medlin, and Rémi Dingreville. Disconnection-mediated transition in segregation structures at twin boundaries. *The Journal of Physical Chemistry Letters*, 12(29):6875–6882, 2021.

[34] Linlin Li, Zhiming Li, Alisson Kwiatkowski da Silva, Zirong Peng, Huan Zhao, Baptiste Gault, and Dierk Raabe. Segregation-driven grain boundary spinodal decomposition as a pathway for phase nucleation in a high-entropy alloy. *Acta Materialia*, 178:1–9, 2019.

[35] R.D. Kamachali, A. Kwiatkowski da Silva, E. McEniry, B. Gault, J Neugebauer, and D. Raabe. Segregation-assisted spinodal and transient spinodal phase separation at grain boundaries. *npj Comput Mater*, 6:191, 2020.

[36] Linlin Li, Reza Darvishi Kamachali, Zhiming Li, and Zhefeng Zhang. Grain boundary energy effect on grain boundary segregation in an equiatomic high-entropy alloy. *Physical Review Materials*, 4(5):053603, may 2020.

[37] M. H. Burden and J. D. Hunt. Cellular and dendritic growth. II. *Journal of Crystal Growth*, 22(2):109–116, 1974.

[38] M. Gäumann, R. Trivedi, and W. Kurz. Nucleation ahead of the advancing interface in directional solidification. *Materials Science and Engineering A*, 226-228:763–769, 1997.

[39] Wei Zhang, Ali Chabok, Bart J. Kooi, and Yutao Pei. Additive manufactured high entropy alloys: A review of the microstructure and properties. *Materials and Design*, 220:110875, 2022.

[40] Mengyao Zheng, Chuanwei Li, Xinyu Zhang, Zhenhua Ye, Xudong Yang, and Jianfeng Gu. The influence of columnar to equiaxed transition on deformation behavior of FeCoCrNiMn high entropy alloy fabricated by laser-based directed energy deposition. *Additive Manufacturing*, 37:101660, 2021.

[41] Hongge Li, Yongjiang Huang, Jianfei Sun, and Yunzhuo Lu. The relationship between thermo-mechanical history, microstructure and mechanical properties in additively manufactured CoCrFeMnNi high entropy alloy. *Journal of Materials Science and Technology*, 77:187–195, 2021.

[42] David W. Hoffman and John W. Cahn. A vector thermodynamics for anisotropic surfaces. I. Fundamentals and application to plane surface junctions. *Surface Science*, 31(C):368–388, 1972.

[43] G.S. Rohrer. Grain boundary energy anisotropy: a review. *J Mater Sci*, 46:5881–5895, 2011.

[44] Yong Li, Bao Nam Ngo-Dinh, Jürgen Markmann, and Jörg Weissmüller. Evolution of length scales and of chemical

heterogeneity during primary and secondary dealloying. *Acta Materialia*, 222:117424, 2022.

[45] G. Laplanche, S. Berglund, C. Reinhart, A. Kostka, F. Fox, and E.P. George. Phase stability and kinetics of σ-phase precipitation in CrMnFeCoNi high-entropy alloys. *Acta Materialia*, 161:338–351, 2018.

[46] Guillaume Bracq, Mathilde Laurent-Brocq, Loïc Perrière, Rémy Pirès, Jean Marc Joubert, and Ivan Guillot. The fcc solid solution stability in the Co-Cr-Fe-Mn-Ni multi-component system. *Acta Materialia*, 128:327–336, 2017.

[47] B. Schuh, F. Mendez-Martin, B. Völker, E. P. George, H. Clemens, R. Pippan, and A. Hohenwarter. Mechanical properties, microstructure and thermal stability of a nanocrystalline cocrfemnni high-entropy alloy after severe plastic deformation. *Acta Materialia*, 96:258–268, 9 2015.

[48] Reza Darvishi Kamachali and Lei Wang. Elastic energy of multi-component solid solutions and strain origins of phase stability in high-entropy alloys. *Scripta Materialia*, 206:114226, 2022.

[49] M. Vaidya, K.G. Pradeep, B.S. Murty, G. Wilde, and S.V. Divinski. Bulk tracer diffusion in CoCrFeNi and CoCrFeMnNi high entropy alloys. *Acta Materialia*, 146:211–224, 2018.

[50] Kazuki Sugita, Naoki Matsuoka, Masataka Mizuno, and Hideki Araki. Vacancy formation enthalpy in CoCrFeMnNi high-entropy alloy. *Scripta Materialia*, 176:32–35, 2020.

[51] Marcel Glienke, Mayur Vaidya, K. Gururaj, Lydia Daum, Bengü Tas, Lukasz Rogal, K. G. Pradeep, Sergiy V. Divinski, and Gerhard Wilde. Grain boundary diffusion in CoCrFeMnNi high entropy alloy: Kinetic hints towards a phase decomposition. *Acta Materialia*, 195:304–316, 2020.

[52] F.J. Ye, T. Zhu, Q.Q. Wang, Y.M. Song, H.Q. Zhang, P. Zhang, P. Kuang, R.S. Yu, X.Z. Cao, and B.Y. Wang. Positron annihilation study of open volume defects and cr segregation in deformed cocrfemnni alloy. *Intermetallics*, 149:107670, 10 2022.